







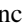





Energy variation of double K -shell photoionization of Ne

S. H. Southworth ¹, S. Li ¹, D. Kouletianos ^{1,*}, G. Doumy ¹, L. Young ^{1,2}, D. A. Walko,³ R. Püttner ⁴, D. Céolin ⁵, R. Guillemin ^{5,6}, I. Ismail,^{5,6} O. Travnikova ^{5,6}, M. N. Piancastelli,⁶ M. Simon ^{5,6}, S. T. Manson ⁷ and T. W. Gorczyca ⁸

¹Chemical Sciences and Engineering Division, Argonne National Laboratory, Lemont, Illinois 60439, USA

²The James Franck Institute and Department of Physics, The University of Chicago, Chicago, Illinois 60637, USA

³Advanced Photon Source, Argonne National Laboratory, Lemont, Illinois 60439, USA

⁴Fachbereich Physik, Freie Universität Berlin, Arnimallee 14, D-14195 Berlin, Germany

⁵Synchrotron SOLEIL, l'Orme des Merisiers, Saint-Aubin, BP 48, 91192 Gif-sur-Yvette, France

⁶Sorbonne Université, CNRS, Laboratoire de Chimie Physique-Matière et Rayonnement, LCPMR, F-75005 Paris, France

⁷Department of Physics and Astronomy, Georgia State University, Atlanta, Georgia 30303, USA

⁸Department of Physics, Western Michigan University, Kalamazoo, Michigan 49008, USA



(Received 14 October 2022; revised 17 January 2023; accepted 30 January 2023; published 21 February 2023)

We report on an experimental and theoretical study of double K -shell photoionization of Ne over the 2.3–8.5 keV x-ray energy range. The ratio of double-to-single K -shell photoionization cross sections was determined experimentally by measuring the relative rates of the $KK - KL_{2,3}L_{2,3}$ (2D) Auger hypersatellite and the $K - L_{2,3}L_{2,3}$ (1D) diagram Auger transitions. By scaling the hypersatellite-diagram Auger-electron ratios to KK/K cross-section ratios, comparison was made with theoretical cross-section ratios of He-like Ne^{8+} determined by the R matrix with pseudostates method. The experimental Ne and theoretical Ne^{8+} cross-section ratios show similar variations with energy, but the experimental ratios systematically exceed the calculated ratios and also show a lower threshold energy for double K -shell photoionization onset compared to the computed Ne^{8+} threshold. The discrepancy is attributed to effects of L -shell electrons not included in the He-like Ne^{8+} calculations. Quantified scaling with nuclear charge Z along the He-like isoelectronic sequence indicates that the measured 10-electron $Z = 10$ double K -shell photoionization cross section behaves like the computed He-like $Z = 8.9$ cross section, suggesting an effective nuclear screening parameter of $s_L = 1.1$ by the additional eight outer L -shell electrons. Experimental results for the energy variations of Auger electron transitions from other multielectron hole states are also discussed.

DOI: [10.1103/PhysRevA.107.023110](https://doi.org/10.1103/PhysRevA.107.023110)

I. INTRODUCTION

Studies of double photoionization by a single photon are of singular importance in atomic physics for two reasons. First, since the photon only interacts with a single atomic electron [1], the second electron can only be emitted owing to correlation among the atomic electrons. Thus double ionization provides information on many-body interactions in atoms. Second, the final state of the double-photoionization process is comprised of three charged particles, the residual ion and the two photoelectrons, and this three-body continuum Coulomb problem is one of the most important problems in both classical and quantum physics [2]. The He atom with only two electrons is the ideal system to study this double-ionization process. Double photoionization of He by a single photon and the variation with photon energy of the ratio of the double- and single-photoionization cross sections have been well studied experimentally [3–6] and by a number of

theoretical treatments [7–18]. The studies of He have motivated general theoretical investigations of KK/K , the ratio of double-to-single K -shell photoionization cross sections of He-like ions, Z scaling of the cross sections, and parametrization of the shape of KK/K as a function of photon energy [17–22]. Studying two-electron atoms or ions is simple in the sense that there are no outer-shell electrons to perturb the results. However, the KK/K ratios in such systems are typically obtained using photoion spectroscopy, so that the measured single-ionization cross section includes the photoionization-plus-excitation channels in addition to the main line where the ion is left in the $1s$ state. By using photoelectron spectroscopy to measure satellite-to- $1s$ ratios, it was found that the inclusion of these satellite processes increases the intensity of the single-ionization cross section for He by the order of 10% of the main line [23]. Furthermore, higher- Z He-like ions are challenging to study experimentally, because this requires both making the ions with sufficient densities and having an intense, high-energy photon beam available. In addition, the ions created could be in long-lived metastable $1s2s$ states that would make the results difficult to interpret. One way around these difficulties is to look at KK/K ratios in neutral atoms. This introduces the perturbation of the outer electrons on the KK/K cross sections and ratios [24–26]. However, the existence of the outer-shell electrons engenders x-ray and Auger

*Present address: Center for Free-Electron Laser Science, Deutsches Elektronen-Synchrotron DESY, Notkestrasse 85, 22607 Hamburg, Germany and Department of Physics, Universität Hamburg, Luruper Chaussee 149, 22761 Hamburg, Germany.

transitions following the photoionization process, and high-resolution spectroscopy can separate the various processes. Thus measurements of KK/K for heavier neutral atoms have been determined from ratios of hypersatellites (from double- K vacancies) and diagram (from single- K vacancies) line intensities in x-ray emission [24,27–29] and Auger electron spectra [30–34]. Auger electron lines that are described as “diagram,” “satellite,” and “hypersatellite” transitions are discussed in Refs. [35,36].

Analysis of the high-resolution Auger electron spectrum of Ne has revealed rich structure from K^{-2} , $K^{-2}V$, $K^{-1}L^{-1}V$, and other many-electron vacancy states produced in photoionization by 2.3 keV x rays [33,34]. The notation K^{-2} refers to the Ne^{2+} configuration $1s^0 2s^2 2p^6$ with an empty K shell, $K^{-2}V$ refers to a Ne^+ configuration $1s^0 2s^2 2p^6 nl$ with an empty K shell and one electron promoted to a valence orbital nl ($n \geq 3$), and $K^{-1}L^{-1}V$ refers to a Ne^+ configuration with one K -shell electron and one L -shell electron removed and one electron promoted to a valence orbital nl ($n \geq 3$). We adopt this notation from Refs. [33,34], where it is used to identify multielectron hole states and their Auger-electron decay transitions.

To measure the variation with photon energy of the KK/K ratio of Ne, we have recorded high-resolution Auger electron spectra over the 2.3–8.5 keV x-ray energy range. The Auger electron spectra are similar to the electron spectrum recorded at 2.3 keV and the transitions identified in Refs. [33,34]. The KK/K ratio is determined from the intensity ratio of the hypersatellite transition $1s^{-2} \rightarrow 1s^{-1} 2p^{-2} (^2D)$ to the diagram transition $1s^{-1} \rightarrow 2p^{-2} (^1D)$ after scaling the Auger branching ratios to the double- and single-photoionization cross sections. The measured KK/K ratios are compared with calculations on He-like Ne^{8+} using the R matrix with pseudostates (RMPS) method [37]. This RMPS method was employed because it has been successfully applied to calculations of two-electron photoexcitation and double photoionization of He and endohedral $\text{He}@C_{60}$ [37–39]. Here we apply the RMPS method to double K -shell photoionization of He-like Ne^{8+} to compare with the present measurements on neutral Ne and with RMPS calculations for He and He-like Be^{2+} .

We also measured the variation with photon energy of the ratio of the satellite Auger transitions $1s^{-1} 2p^{-1} 3p \rightarrow 2p^{-2}$ to the diagram transition $1s^{-1} \rightarrow 2p^{-2} (^1D)$. In addition, the double core-hole transitions $1s^{-2} 3p \rightarrow 1s^{-1} 2p^{-2} (^2D) 3p$ and $1s^{-2} 3s \rightarrow 1s^{-1} 2p^{-2} (^2D) 3s$ which are observed in the Auger spectrum [33,34] induced by 2.3 keV x rays are not observed above background in the 6–8.5 keV x-ray energy range since the cross sections for producing them are too small in that region. In summary, the observed intensities of Auger lines from different inner-shell vacancy states and their ratios clearly demonstrate significant variations with x-ray energy.

Using the multiconfiguration Dirac-Fock (MCDHF) method, Chen calculated Auger transition rates and fluorescence yields for double- K -hole states of Ne and selected higher- Z atoms [40]. More recent calculations of double core hole states and Auger decay transitions of Ne are reported in Refs. [41–44]. In one of the first experiments using ultraintense femtosecond x-ray free-electron lasers, double K -shell ionization of Ne was produced by sequential absorption of two photons from the same pulse prior to Auger decay of the first core hole

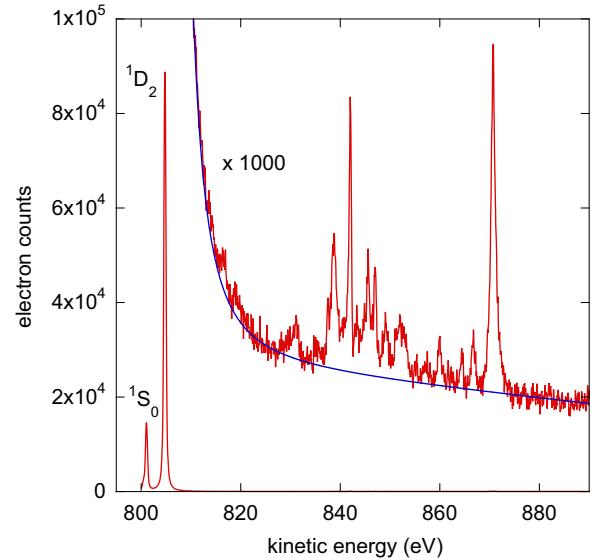


FIG. 1. Auger-electron spectrum of Ne obtained by summing measurements made at six photon energies between 6 and 8.5 keV. The diagram Auger lines $K - L_{2,3}L_{2,3} {}^1S_0$ and 1D_2 are indicated at 800.6 eV and 804.3 eV, respectively [48]. The energy region between 810 and 890 eV is scaled by $\times 1000$ to show the structure from KK hypersatellites and other Auger transitions from multielectron hole states [33,34]. The blue curve under the structure expanded by $\times 1000$ is a fit to the Lorentzian tail of the 1D_2 peak.

[45]. We note that the KK/K measurements and calculations reported in the present paper are for the case of single-photon absorption in the weak-field regime where the production of KK and other multielectron hole states is effected only *via* electron correlation.

Section II of this paper describes the experimental instrumentation and methods, Sec. III describes the theoretical and calculational methods, and Sec. IV discusses the measured and calculated results. Conclusions and suggestions for future research are given in Sec. V.

II. EXPERIMENT

Two sets of measurements of the Ne Auger spectrum were recorded using Scienta EW4000 hemispherical electron analyzers. Measurements over the 2.3–6.5 keV x-ray range were made using a Si(111) monochromator with bandwidths < 1 eV on the GALAXIES beamline at the SOLEIL synchrotron facility [46]. Measurements at higher x-ray energies, 6–8.5 keV, were made using a Si(111) monochromator with bandwidths 1.1–1.6 eV on beamline 7-ID at the Advanced Photon Source (APS) [47]. Figure 1 shows an overview of the Auger spectrum obtained by summing the six measurements made at 6.0, 6.5, 7.0, 7.5, 8.0, and 8.5 keV at the APS. The spectrum in Fig. 1 is dominated by the diagram transitions $1s^{-1} \rightarrow 2p^{-2} ({}^1S_0)$ and $({}^1D_2)$ [48]. Expanding the scale by $\times 1000$ reveals the hypersatellites and other satellites in the 810–890 eV range that are identified in Refs. [33,34]. The Auger electron measurements made at SOLEIL and APS used the same spectrometer parameters, 200 eV pass energy with a 0.5 mm entrance slit over 800–890 eV with 0.05 eV

steps, as was used for the 2.3 keV measurements reported in Refs. [33,34]. To check for variations of the detection efficiencies of the electron spectrometers, measurements over the 800–890 eV kinetic energy range were made using Ar 1s photoelectrons at SOLEIL and Kr 1s photoelectrons at APS. Significant variations of the detection efficiencies were not found, so no corrections were made to the Ne data. We note that the $\text{Ne}^+ 1s^1 2s^2 2p^6$ and $\text{Ne}^{2+} 1s^0 2s^2 2p^6$ states produced by single- and double-*K*-shell photoionization, respectively, are both spherically symmetric, i.e., unaligned. The diagram and hypersatellite Auger transitions are therefore ejected isotropically and their intensity ratios are unaffected by angular distribution effects [49]. More generally, however, $K^{-2}V$ and $K^{-1}L^{-1}V$ initial states could be aligned and their Auger transitions could eject electrons with nonzero anisotropy parameters β [49]. The entrance lenses of the electron analyzers were parallel to the x-ray polarization, i.e., at a polar angle of 0° , at both the SOLEIL and APS beamlines. Nonzero β parameters would therefore affect the intensities of detected electrons. We rely on the detailed analysis of Refs. [33,34] for assignments of the initial and final states of the Auger transitions studied in the present paper.

Figure 1 shows a curve below the satellite structure from fitting the Lorentzian tail of the (1D_2) diagram peak. Lorentzian tails were subtracted from all of the Auger spectra to obtain satellite spectra such as that plotted in Fig. 2. Figure 2 compares the satellite spectrum summed over the 6–8.5 keV measurements plotted in Fig. 1 with a new 2.3 keV spectrum recorded at the GALAXIES beamline. The satellite spectra in Fig. 2 are in good overall agreement with the 2.3 keV spectrum analyzed in Refs. [33,34]. Three peaks in Fig. 2(a) are labeled A: $1s^{-1}2p^{-1}3p \rightarrow 2p^{-2}$, B: $1s^{-2} \rightarrow 1s^{-1}2p^{-2}(^2D)$, and C: $1s^{-2}3p \rightarrow 1s^{-1}2p^{-2}(^2D)3p$ and $1s^{-2}3s \rightarrow 1s^{-1}2p^{-2}(^2D)3s$. Peak A consists of two closely spaced transitions, namely the dominating transition $1s^{-1}2p^{-1}(H)3p \rightarrow 2p^{-2}(^1D)$ at 841.7 eV and the less intense transition $1s^{-1}2p^{-1}(L)3p \rightarrow 2p^{-2}(^1S)$ at 841.4 eV [34]. The initial states of peak A are $2p \rightarrow 3p$ shakeup states of single *K*-shell photoionization [50] with different coupling of the 1s and the 2p holes, namely to a singlet (*H*) and a triplet (*L*) [34]. For simplicity in the following discussion we label the two overlapping transitions $1s^{-1}2p^{-1}3p \rightarrow 2p^{-2}$. Peak B at 870.4 eV is the strongest hypersatellite [34]. Peak C consists of two transitions at 880.6 eV and 881.7 eV with initial states in which a 1s electron is ejected and a second 1s electron is shaken up to a 3p or 3s orbital [33]. Comparison with the 6–8.5 keV spectrum in Fig. 2(b) shows that the relative heights of peaks A and B have changed and peak C is not observed.

Peak fitting procedures were used to determine the relative intensities of the $1s^{-1} \rightarrow 2p^{-2}(^1D)$ diagram line, the $1s^{-1}2p^{-1}3p \rightarrow 2p^{-2}$ Auger satellites, and the $1s^{-2} \rightarrow 1s^{-1}2p^{-2}(^2D)$ hypersatellite. As discussed in Ref. [33], a novel postcollision interaction effect produces an asymmetric line shape of the hypersatellite, so an asymmetric fitting function was used to determine its peak areas.

III. THEORY

For the present double photoionization calculations, the well-developed *R*-matrix method [51], as implemented in the

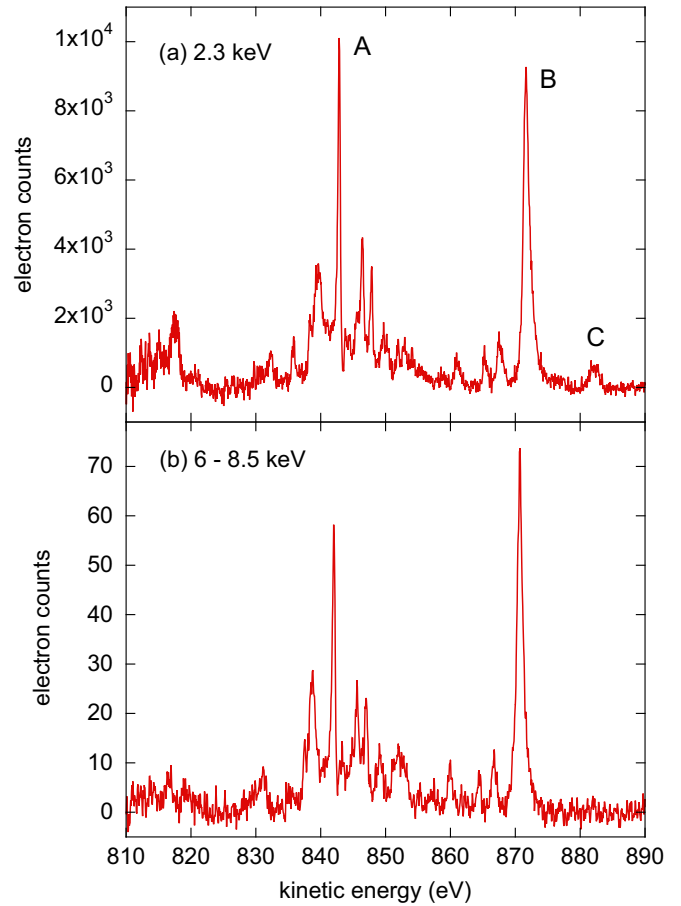


FIG. 2. Ne satellite and hypersatellite Auger spectra measured at (a) 2.3 keV x-ray energy and (b) the sum of six spectra over 6–8.5 keV. The peaks labeled in panel (a) are identified in Ref. [34] as A: $1s^{-1}2p^{-1}3p \rightarrow 2p^{-2}$, B: $1s^{-2} \rightarrow 1s^{-1}2p^{-2}(^2D)$, and C: $1s^{-2}3p \rightarrow 1s^{-1}2p^{-2}(^2D)3p$ and $1s^{-2}3s \rightarrow 1s^{-1}2p^{-2}(^2D)3s$.

popular “Belfast” version of FORTRAN codes [52–54], is applied. These codes have been used extensively over decades to treat numerous elements and ionization stages of the Periodic Table, to benchmark experiment and produce atomic collision data for astrophysics and fusion applications. The normal *R*-matrix approach is to consider the close-coupling equations [55] arising from a free or valence electron coupled to an ionic target state, allowing the treatment of single-ionization processes.

Even in early atomic *R*-matrix calculations [56], however, it was realized that an expanded basis of atomic orbitals consisting of the usual physical orbitals, augmented by additional *pseudo-orbitals*, could be used to model more accurately the electron-ionic target interactions. Appropriately optimized *pseudo-orbitals* can be used to simulate a second continuum electron, giving an approximate representation of a two-electron final-state wave function. No reliable quantitative calculations were then possible, however, because of computational limitations.

In the 1990s there was a huge resurgence in the study of double photoionization of helium, both experimentally and via several independent theoretical methods (see, for instance, a comprehensive review at the time [57]). One of the the-

oretical methods to get renewed attention was the so-called *R matrix with pseudostates* (RMPS) method, originally attempted 30 years earlier [56]. A successful application for treating double photoionization was first carried out by Meyer and Greene using the eigenchannel *R*-matrix codes [10]. Later applications using the Belfast *R*-matrix version were then achieved by Bartschat and co-workers [58–60] and independently by Gorczyca and Badnell [37], giving reasonable double photoionization results in line with the eigenchannel *R*-matrix results [10] and experimental measurements [6]. The Belfast RMPS method [37] is used in the present studies.

RMPS calculations have been applied first and foremost to the double photoionization of helium [37–39], where convergence studies have been carried out and the importance of an appropriate orbital basis representation has been revealed. A pseudostate Laguerre basis [37] used in this work is a discrete representation of the second continuum electron, and unphysical pseudoresonance oscillations occur as a result of this finite basis. Nevertheless, the unphysical artifacts can be minimized by using a larger “box” for the pseudo-orbitals to increase the pseudostate density in energy, but then many more such orbitals are required to allow representation at higher energies. The optimum approach is to settle on the largest orbital basis that is computationally feasible for the available computational ability and then optimize the box size that contains the pseudo-orbitals, which can be facilitated easily by changing the default λ parameter of the $e^{-\lambda r}$ factor in the Laguerre basis. These considerations come into play when discussing the computed cross sections in the following results section.

The RMPS method has also been used to treat other quasi-two-electron cases [39,61–64] by treating only two outer-shell active electrons outside a frozen inner-shell core. For that case, the average effect of the inner-shell electrons is considered for the ionization of the outer two electrons, but no electron promotions from those inner-shell electrons is included. For the present case of 10-electron neon, considering the two inner-shell $1s$ electrons as active instead, we make the approximation that the double photoionization occurs entirely within the inner *K* shell and is so well separated from the outer *L*-shell $2s$ and $2p$ electrons that we can completely ignore the *L*-shell electrons altogether. That is, the double *K*-shell photoionization of 10-electron neutral Ne is here modeled theoretically as the double photoionization of two-electron (pure He-like) Ne^{8+} , disregarding all eight outer *L*-shell electrons altogether. Single and double photoionization cross sections, discussed in the following section, were generated using essentially an identical approach as for the earlier He RMPS calculations [37–39] except that the nuclear charge is changed from $Z = 2$ to $Z = 10$.

At this point, it is worthwhile to discuss the expected validity of the theoretical approximation, which is to assume that the *K*-shell photoionization can be simulated using a two-electron, 10-proton heliumlike Ne^{8+} model. Our first approach was to consider an *R*-matrix approach including all 10 electrons as active. However, the deeply bound nature of the $1s^2 2s^2 2p^6$ neutral neon initial state, relative to the final, doubly ionized $1s^0 2s^2 2p^6$ final ionic state of Ne^{2+} , led to numerical difficulties that have not been solved yet and are part of a continuing investigation into this and other double-

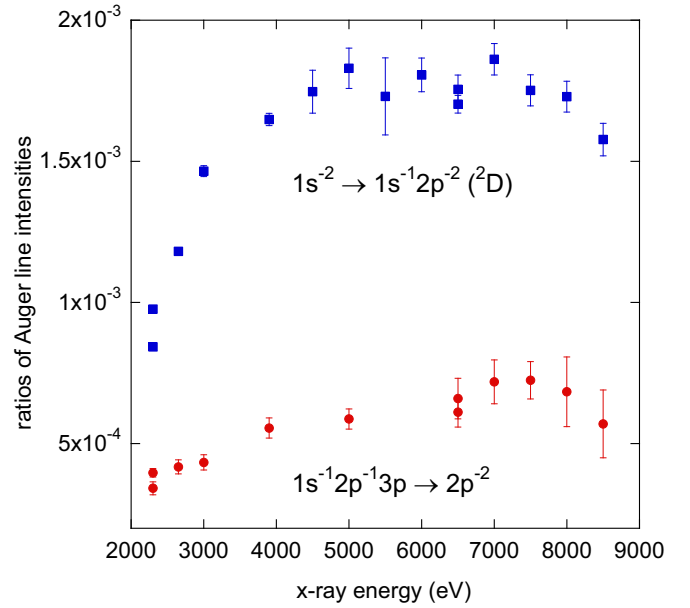


FIG. 3. Ratios of Auger transition rates over the 2.3–8.5 keV x-ray energy range. The ratio of the hypersatellite transition $1s^{-2} \rightarrow 1s^{-1}2p^{-2}(^2D)$ to the diagram transition $1s^{-1} \rightarrow 2p^{-2}(^1D)$ is plotted as blue squares. The ratio of the satellite transitions $1s^{-1}2p^{-1}3p \rightarrow 2p^{-2}$ to the diagram transition $1s^{-1} \rightarrow 2p^{-2}(^1D)$ is plotted as red circles. The error bars are determined from uncertainties in the peak fits.

K-shell ionization studies. A third approach, intermediate to the present Ne^{8+} model and a fuller 10-electron treatment and also a part of that same ongoing investigation, is to treat the eight $2s$ and $2p$ *L*-shell electrons as forming a spherically symmetric charged Gaussian sphere of charge $q = -8e$, giving an effective, independent-particle approximation (IPA) electric field

$$\mathcal{E}(\vec{r}) = \frac{e^2}{4\pi\epsilon_0 r^2} \left(+10 - \int_0^r 4\pi r'^2 dr' [2R_{2s}^2(r') + 6R_{2p}^2(r')] \right),$$

where $R_{nl}(r)$ are the radial wave functions for the $2s$ and $2p$ electrons. This *screened* IPA potential electric field gives rise to a corresponding modified electric potential that can be included in the *R*-matrix inner-region Hamiltonian. Nevertheless, it needs to be stressed that the present two-electron dynamic model is expected from the outset to be a fairly good approximation to the 10-electron neon case due to the significantly different spatial distributions of the two *K*-shell electrons and the eight *L*-shell electrons; the double *K*-shell ionization largely takes place near a 10-proton nucleus long before the two photoelectrons emerge from the *K* shell, through the *L* shell, to $r \rightarrow \infty$.

IV. RESULTS AND DISCUSSION

A. Experimental results

From peak fitting, the relative areas of the Auger satellite and hypersatellite peaks labeled A and B in Fig. 2 with respect to the 1D diagram line in Fig. 1 are plotted versus x-ray energy in Fig. 3. Note that the Auger rates of the hypersatellite are about three times larger than for the Auger satellite, although

the peak intensities in Fig. 2 are rather similar. This is mainly due to a significantly different lifetime broadening [33]. Both ratios show a gradual rise with energy and broad maxima. The hypersatellite-diagram ratio shows a larger variation with energy and a different shape than the Auger-satellite-diagram ratio. Also, as noted earlier, peak C in Fig. 2 from the $1s^{-2}3p$ and $1s^{-2}3s$ shakeup hole states is not observed in the 6–8.5 keV range. While peak C is clearly observed at 2.3 keV, both here and in the measurements of Refs. [33,34], its intensity decreases with increasing x-ray energy until it is indiscernible from background at approximately 5 keV. It is thus clear that the photoionization cross sections for these shakeup hole states decrease more rapidly with energy than the hole states shown in Fig. 3, thereby showing that different electron correlations, with different energy dependences, are involved in the photoionization processes that produce the various initial hole states.

To convert the hypersatellite-diagram ratios to KK/K cross-section ratios, the branching ratios from $1s^{-2}$ and $1s^{-1}$ hole states to the respective final states are needed. We follow the procedure used in Ref. [32] with the exception of using the measured branching ratio, 0.549(16), of the $1s^{-2} \rightarrow 1s^{-1}2p^{-2}(^2D)$ hypersatellite transition from Table II of Ref. [34]. As in Ref. [32], we estimate the single-Auger yields for $1s^{-1}$ and $1s^{-2}$ hole states to be 0.9267(21) and 0.90(5), respectively. We also use 0.6086(15) from Ref. [48] as the single-Auger branching ratio for the $1s^{-1} \rightarrow 2p^{-2}(^1D)$ diagram transition. This results in a scale factor of 1.1414 to convert Auger hypersatellite-diagram intensity ratios to KK/K cross-section ratios. The measured and calculated KK/K ratios are plotted in Fig. 4, but we defer discussion of the results to Sec. IV C after the calculations are discussed in more detail. The uncertainties on the KK/K measurements in Fig. 4 are the combined uncertainties from the hypersatellite peak fits and the uncertainty in the scale factor.

B. Theoretical results

The orbital basis included 114 orbitals spanning from $1s$, $2s$, and $2p$ physical orbitals to $\overline{3s}$, $\overline{3p}$, ..., $\overline{30d}$, $\overline{30f}$ pseudo-orbitals, i.e., up through $n_{\max} = 30$ and $l_{\max} = 3$. Given this fairly large orbital and configuration basis size, it is quite important to choose appropriate pseudoorbitals, with moderation through the λ parameter used to constrict the radial range of the Laguerre orbitals. As seen in Fig. 5 for double photoionization of He, when the λ parameter is varied from 1 to 3, there is a corresponding shrinking of the R -matrix radius (the box size), allowing a dense enough representation to higher energy at the expense of yielding a less-dense mesh near threshold. For $\lambda = 1$, a containing atomic box of radius $R_A = 76$ a.u. gives a cross section that is essentially smooth near threshold, but the representation breaks down at a photon energy of 200 eV—less than the full energy range of the neutral Ne experiment. By setting $\lambda = 3$ instead, the box size is reduced to $R_A = 25$ a.u. and reliable double photoionization cross sections are calculated up to about 1400 eV, at the expense of increasing somewhat the unphysical oscillations near threshold.

To understand this behavior most easily, consider the energy levels and energy density of a one-dimensional infinite

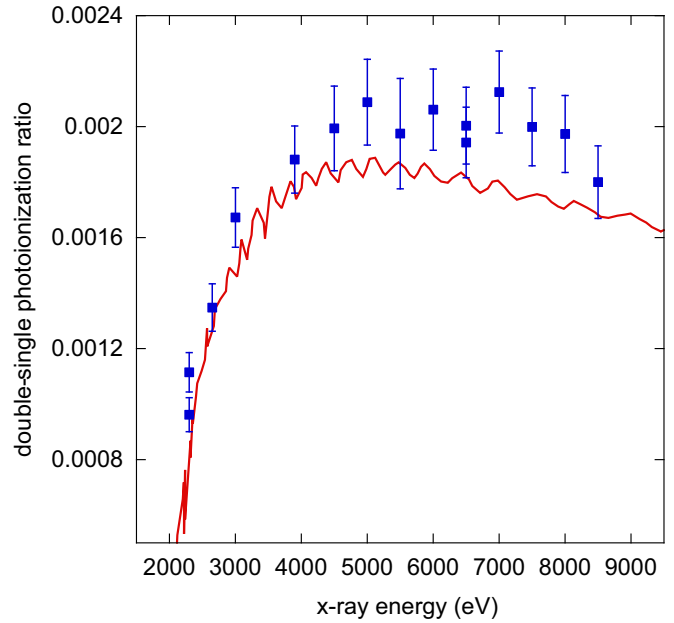


FIG. 4. Double-to-single K -shell photoionization cross-section ratios measured over 2300–8500 eV (blue squares) compared with theoretical ratios (red curve) from R matrix with pseudostates (RMPS) calculations of He-like Ne^{8+} . The RMPS curve has been shifted to lower energy by 695 eV to correct for the difference in the double K -shell ionization energies of 10-electron Ne (1863 eV [31]) and of Ne^{8+} (2558 eV [65]).

square well of width L (a simplified model of an atomic interaction):

$$E = \frac{\hbar^2 n^2}{8m L^2}$$

and

$$\rho(E) = dn/dE = \frac{L}{\hbar} \sqrt{2m/E} = \frac{4m L^2}{\hbar^2 n},$$

where \hbar is Planck's constant. From the energy density expression, it is easily seen that, for any principal quantum number n that counts the number of nodes of the various orbitals, the energy density is greater for larger box sizes L . On the other hand, the energy expression evaluated at the highest orbital $n = n_{\max} = 30$ is reduced as L is increased, meaning the expansion is only valid up to a smaller maximum energy. As seen in Fig. 5, shrinking the box from 76 a.u. to 25 a.u. decreases the energy density near threshold and increases the pseudo-orbital oscillations in between the sparser energy levels, but it also allows an expanded energy range of applicability, from 200 eV to 1400 eV. Regarding other convergence factors, an earlier study of oxygen double photoionization [39] looked first at He and demonstrated that unphysical oscillations can also be reduced by increasing the number of pseudo-orbitals and continuum functions for a given box size $R_A = 75$ a.u., showing that large oscillations for $n_{\max} = 12$ were reduced to essentially a smooth cross section for $n_{\max} = 30$.

As a final note, the extension to higher energy via an increase of the screening parameter λ has been demonstrated in Fig. 5 for He, versus the present case of Ne^{8+} , because the

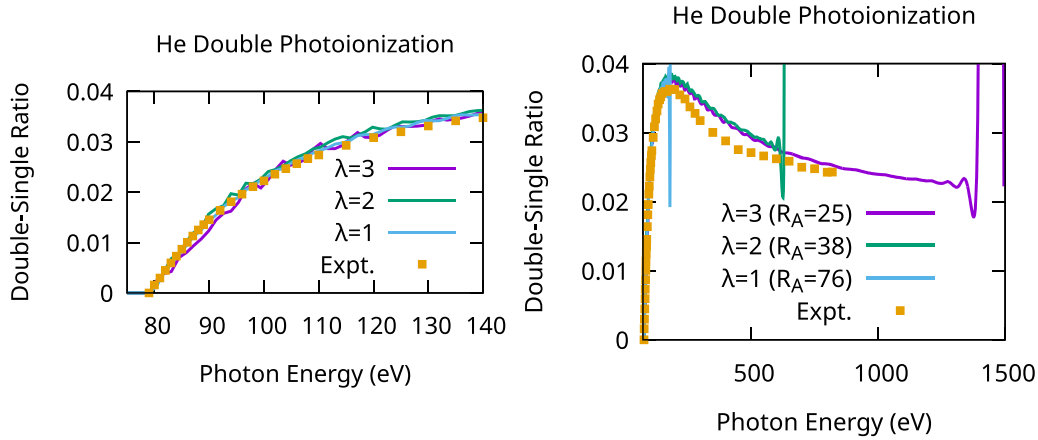


FIG. 5. Double-to-single K -shell photoionization cross-section ratios computed from R matrix with pseudostates (RMPS) calculations of He, showing an expanded photoelectron energy range of applicability as the R -matrix box size, R_A (in a.u.), is varied *via* the parameter λ of the $e^{-\lambda r}$ factor in the Laguerre basis. The higher-energy range of applicability as λ is increased, and the box size is decreased, for a given basis size of 114 physical orbitals and pseudo-orbitals (right), is countered by an increase in unphysical pseudostate oscillations near threshold (left).

available experimental data for He [5,66] extends to higher scaled photon energies than for Ne^{8+} (see the further energy scaling discussion below), and so it was necessary to extend to $\lambda = 3$ in order to extend the applicability of the RMPS method to span the range of the He experimental energy data. The present Ne^{8+} experimental results, on the other hand, extend instead up to a photon energy for which it was possible to obtain reliable RMPS results for $\lambda = 2$, which is used from here on. Since the energies have a Z^2 scaling factor, the energy range applicability between neutral He and Ne^{8+} cannot be compared directly, but the same general behavior of extending to higher energies via increased λ applies to Ne^{8+} as well as for He.

C. Comparison of experimental and theoretical results

Having established a reliable set of orbitals for He, the exact same orbitals, optimized instead on a two-electron, 10-proton He-like system, and the exact same configurations are used for the Ne^{8+} double photoionization calculations. Cross sections are shown in Fig. 6 for single K -shell photoionization, photoionization-excitation to $n = 2$ and $n = 3$, and double photoionization, which is determined by summing the partial photoionization-excitation cross sections to all pseudostates with energies above the double ionization threshold of 2558 eV [65]. The double photoionization cross section of Ne^{8+} computed using the intermediate-energy R -matrix method (IERM) [18], which has been smoothed via a seventh-order polynomial fit, is seen to agree with the present RMPS results. Also shown are the compiled data from Hartree-Slater calculations [67] for the background (resonance-free) $1s$ photoionization that align quite well with the present R -matrix cross section away from resonance. Note that the direct $1s$ photoionization cross section is two orders of magnitude greater than the photoionization-excitation cross sections, so that the double-to-single ratio computed here—the double photoionization cross section divided by the direct $1s$ cross section—would not be changed much by also including the other channel contributions in the denominator.

The measured and calculated double-to-single cross-section ratios are plotted in Fig. 4 after shifting the RMPS curve by -695 eV to correct for the difference in the double K -shell ionization energies of 10-electron Ne (1863 eV [31]) and of Ne^{8+} (2558 eV [65]). The shapes of the energy variations are similar, but the measured ratios exceed the calculations. A possible explanation for this discrepancy is the additional shielding provided by the eight L -shell electrons that are not included in the RMPS calculations for He-like Ne^{8+} . Similar differences between measured KK/K ratios of neutral atoms and calculations on He-like ions of Mg, Al, and Si were reported by Hoszowska *et al.* [24]. To explore the effects of outer shell electrons, Kheifets *et al.* [25] derived a K -shell double photoionization scaling curve for neutral atoms and Yerokhin *et al.* [26] calculated double K -shell photoionization cross sections of neutral medium- Z atoms. The KK/K results for Ne plotted in Fig. 4 offer another example for investigation of the effects of outer-shell electrons.

In order to obtain a more meaningful comparison between the experimental KK/K ratio for 10-electron neutral Ne with the computed two-electron Ne^{8+} ratio, it is useful to first investigate the behavior of the ratio along the He-like isoelectronic sequence. Consider first the onset energy for double K -shell photoionization of a He-like atom. It is well known [68] that a variational calculation for the total binding energy of two electrons to a nucleus of charge $+Z$, using a two-electron trial wave function of the form $e^{-(Z-s)r_1} e^{-(Z-s)r_2}$, yields an optimized value of the $1s - 1s$ screening parameter $s = \frac{5}{16} = 0.3125$, giving a fairly good Z -scaling approximation of a factor of $(Z - s)^2$ for the double-ionization threshold. (An improved screening parameter $s = 0.291$ was found to fit the data best for the scaled ionization threshold.) The cross-section ratio scaling, on the other hand, involves the ratio of two ionizations to one ionization. Now the double-ionization process can only occur *via* correlation, i.e., the electron-electron interaction term in the many-body Schrödinger equation. Thus, if the Schrödinger equation is recast with $r_i \rightarrow Zr_i$ and $E \rightarrow E/Z^2$, the equation is invariant

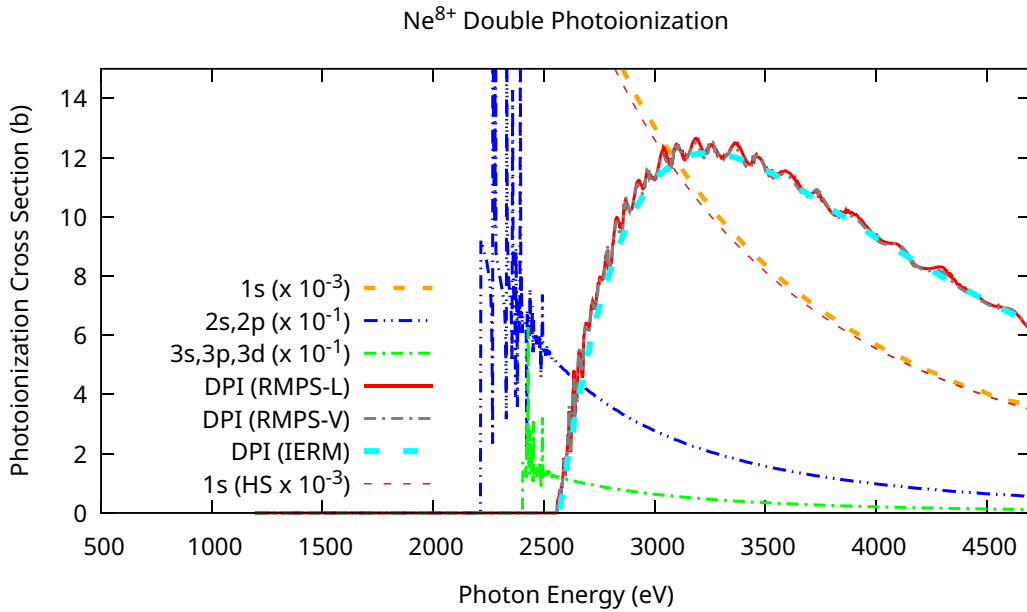


FIG. 6. Single and double *K*-shell RMPS photoionization cross sections for He-like Ne^{8+} , showing characteristic pseudoresonance oscillations in the weaker double-photoionization cross section, which is computed by summing the partial photoionization-ionization cross sections to all final target channels with energies lying above the Ne^{8+} double-ionization channel of 2558 eV [65]. The double photoionization cross section is shown using both the length and velocity forms of the dipole operator, indicating a high degree of reliability in the computed accuracy, within the finite and discrete pseudostate representation of the second ionizing electron. Also shown are IERM double photoionization cross sections [18] and Hartree-Slater $1s$ photoionization cross sections [67].

except for the electron-electron term which acquires a factor of $1/Z$. This means that the correlation and the matrix element causing the double ionization scales as $1/Z$ compared to the single ionization so that the cross-section ratio itself scales as $1/Z^2$ [19]. Indeed, the scaled ratios versus scaled photon energies plotted in Fig. 7 for He, Be^{2+} , and Ne^{8+} show remarkably close agreement, becoming nearly identical for

larger Z as seen by comparing the curves for Be^{2+} and Ne^{8+} . The obvious scaling seen here suggests a simple way to view the comparison between the actual neutral neon double *K*-shell photoionization and the Ne^{8+} RMPS approximation; the actual 10-electron neon case is surely screened to some extent by the additional eight *L*-shell electrons. If we choose the secondary screening parameter due to the eight *L*-shell electrons

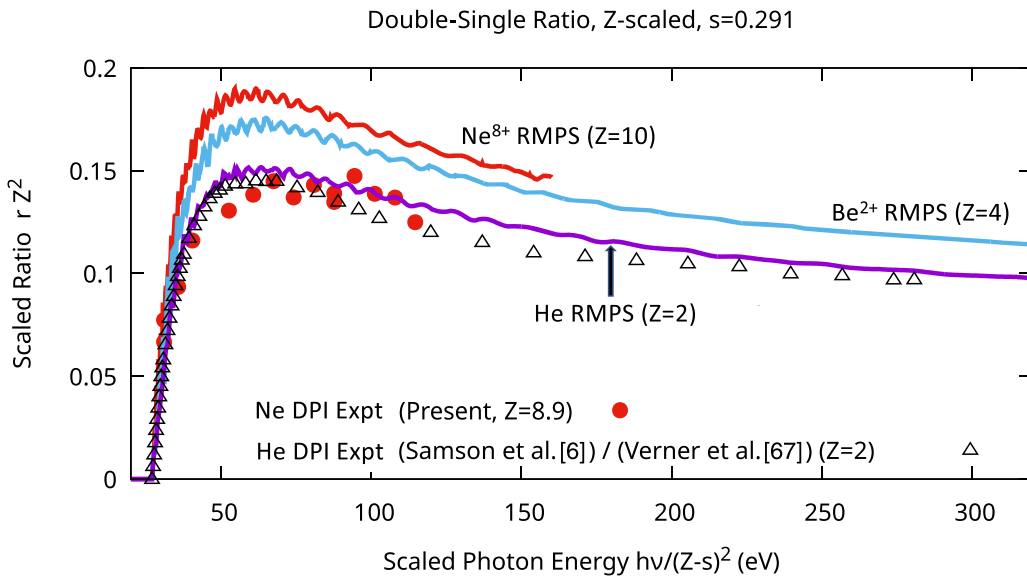


FIG. 7. Scaled double-to-single *K*-shell photoionization cross-section ratios for He and He-like Be^{2+} and Ne^{8+} , compared to earlier He experiments ($Z = 2$, double cross section [6] divided by single $1s$ Hartree-Slater results [67]) and present Ne experimental ratios ($Z = 8.9$). The effective $1s - 1s$ mutual *K*-shell screening parameter of $s = 0.291$ was used rather than the variational calculated result of $s = 0.3125$ [68].

as $s_L = 1.1$, then scaling the energies by $1/(Z - s_L - s)^2 = 1/(8.9 - s)^2$ and the ratios by $(Z - s_L)^2 = (8.9)^2$ aligns the scaled threshold energies extremely well but brings the scaled ratio to a value closer to He than Ne⁸⁺. This suggests that the scaling parameter relationships for the energies and ratios themselves behave somewhat differently for neutral Ne, most likely due to the additional eight *L*-shell electrons introducing more complicated effects.

In a general sense, the problem of the contribution of outer electrons to inner-shell photoionization has been studied some decades ago. This earlier work showed that single-ionization cross sections of inner shells were hardly affected by the removal of outer-shell electrons; see, e.g., Ref. [69] and references therein. The understanding of this phenomenology was based upon Gauss's law and the fact that $\langle r \rangle$ for outer subshells is very much larger than for inner subshells. From a numerical point of view, the screening described above is extremely small. For the double ionization, similar considerations should apply.

V. CONCLUSION

The ratio of double to single *K*-shell ionization of the Ne atom has been measured over a broad range of x-ray energies using high-resolution Auger electron spectroscopy to pinpoint the vacancies produced by the incident x ray. In addition, calculations were performed using the *R* matrix with pseudostates methodology on Ne⁸⁺ in which the pseudostates mocked up the second electron in the double-ionization process. Despite being performed on Ne⁸⁺, the calculations were in rather good agreement with the experimental results on neutral Ne in both magnitude and energy dependence. This implies that the eight *L*-shell electrons of the Ne atom have relatively little to do with the *KK/K* ratio in Ne and, by extension, in other heavier atoms. Of course, it would be extremely useful to extend the calculations to the 10-electron system to understand in detail the roll of the *L*-shell electrons.

Based on the present results and previous experimental and theoretical results, it was found that, to an excellent approximation, the *KK/K* ratio scales as $1/Z^2$. This scaling was explained theoretically based on the relative magnitude of the electron-electron correlation term in the Hamiltonian versus the electron-nuclear potential. Given this scaling, it would be most helpful to look at the situation for higher-*Z* atoms to corroborate the understanding of this scaling. It would also be of interest to go to heavier systems to examine the possibility of relativistic interactions altering the systematics.

In addition to the double ionization *KK* channels observed experimentally, satellite channels, e.g., $1s^{-1}2p^{-1}3p$ (shakeup) and $1s^{-2}3p$ (shakeoff + shakeup), were observed along with their energy dependence; it was found that the various satellite channels exhibited rather different energy dependences. Since satellite photoionization channels are only possible because of the electron-electron interaction, i.e., due to correlation, it is evident that the effects of the correlation can be very different in the various satellite transitions. A more detailed study of these satellite photoionization channels associated with *K*-shell ionization in Ne and other atoms should yield a wealth of information of many-body interactions in photoionizing transitions.

ACKNOWLEDGMENTS

This work was supported by the US Department of Energy, Office of Science, Basic Energy Sciences, Chemical Sciences, Geosciences, and Biosciences Division. The experiments were conducted in part at the GALAXIES beam line of the synchrotron radiation facility SOLEIL, France (Project No. 99190144). This research used resources of the Advanced Photon Source, a US Department of Energy (DOE) Office of Science User Facility operated for the DOE Office of Science by Argonne National Laboratory under Contract No. DE-AC02-06CH11357. T.W.G. was supported in part by NASA.

-
- [1] A. F. Starace, in *Handbuch der Physik*, edited by W. Mehlhorn (Springer-Verlag, Berlin, 1982), pp. 1–121.
 - [2] J. Berakdar and J. S. Briggs, *Phys. Rev. Lett.* **72**, 3799 (1994).
 - [3] R. J. Bartlett, P. J. Walsh, Z. X. He, Y. Chung, E.-M. Lee, and J. A. R. Samson, *Phys. Rev. A* **46**, 5574 (1992).
 - [4] J. C. Levin, I. A. Sellin, B. M. Johnson, D. W. Lindle, R. D. Miller, N. Berrah, Y. Azuma, H. G. Berry, and D.-H. Lee, *Phys. Rev. A* **47**, R16 (1993).
 - [5] R. Dörner, T. Vogt, V. Mergel, H. Khemliche, S. Kravis, C. L. Cocke, J. Ullrich, M. Unverzagt, L. Spielberger, M. Damrau *et al.*, *Phys. Rev. Lett.* **76**, 2654 (1996).
 - [6] J. A. R. Samson, W. C. Stolte, Z.-X. He, J. N. Cutler, Y. Lu, and R. J. Bartlett, *Phys. Rev. A* **57**, 1906 (1998).
 - [7] M. Y. Amusia, E. G. Drukarev, V. G. Gorshkov, and M. O. Kazachkov, *J. Phys. B: At. Mol. Phys.* **8**, 1248 (1975).
 - [8] K.-i. Hino, T. Ishihara, F. Shimizu, N. Toshima, and J. H. McGuire, *Phys. Rev. A* **48**, 1271 (1993).
 - [9] M. A. Kornberg and J. E. Miraglia, *Phys. Rev. A* **48**, 3714 (1993).
 - [10] K. W. Meyer and C. H. Greene, *Phys. Rev. A* **50**, R3573(R) (1994).
 - [11] J.-Z. Tang and I. Shimamura, *Phys. Rev. A* **52**, R3413(R) (1995).
 - [12] A. S. Kheifets and I. Bray, *Phys. Rev. A* **54**, R995 (1996).
 - [13] R. C. Forrey, Z.-C. Yan, H. R. Sadeghpour, and A. Dalgarno, *Phys. Rev. Lett.* **78**, 3662 (1997).
 - [14] Y. Qiu, J.-Z. Tang, J. Burgdörfer, and J. Wang, *Phys. Rev. A* **57**, R1489 (1998).
 - [15] T. Pattard and J. Burgdörfer, *Phys. Rev. A* **64**, 042720 (2001).
 - [16] T. Schneider, P. L. Chocian, and J.-M. Rost, *Phys. Rev. Lett.* **89**, 073002 (2002).
 - [17] V. A. Yerokhin and A. Surzhykov, *Phys. Rev. A* **84**, 032703 (2011).
 - [18] M. W. McIntyre, A. J. Kinnen, and M. P. Scott, *Phys. Rev. A* **88**, 053413 (2013).
 - [19] M. A. Kornberg and J. E. Miraglia, *Phys. Rev. A* **49**, 5120 (1994).
 - [20] A. S. Kheifets and I. Bray, *Phys. Rev. A* **58**, 4501 (1998).

- [21] A. I. Mikhailov, I. A. Mikhailov, A. N. Moskalev, A. V. Nefiodov, G. Plunien, and G. Soff, *Phys. Rev. A* **69**, 032703 (2004).
- [22] T. Pattard, *J. Phys. B: At., Mol., Opt. Phys.* **35**, L207 (2002).
- [23] R. Wehlitz, I. A. Sellin, O. Hemmers, S. B. Whitfield, P. Glans, H. Wang, D. W. Lindle, B. Langer, N. Berrah, J. Viefhaus *et al.*, *J. Phys. B: At., Mol., Opt. Phys.* **30**, L51 (1997).
- [24] J. Hozzowska, A. K. Kheifets, J.-C. Dousse, M. Berset, I. Bray, W. Cao, K. Fennane, Y. Kayser, M. Kavčič, J. Szlachetko *et al.*, *Phys. Rev. Lett.* **102**, 073006 (2009).
- [25] A. S. Kheifets, I. Bray, and J. Hozzowska, *Phys. Rev. A* **79**, 042504 (2009).
- [26] V. A. Yerokhin, A. Surzhykov, and S. Fritzsche, *Phys. Rev. A* **90**, 063422 (2014).
- [27] E. P. Kanter, R. W. Dunford, B. Krässig, and S. H. Southworth, *Phys. Rev. Lett.* **83**, 508 (1999).
- [28] R. Diamant, S. Huotari, K. Hämäläinen, C. C. Kao, and M. Deutsch, *Phys. Rev. A* **62**, 052519 (2000).
- [29] M. Oura, H. Yamaoka, K. Kawatsura, K. Takahiro, N. Takeshima, Y. Zou, R. Hutton, S. Ito, Y. Awaya, M. Terasawa *et al.*, *J. Phys. B: At., Mol., Opt. Phys.* **35**, 3847 (2002).
- [30] Ž. Šmit, M. Žitnik, L. Avaldi, R. Camilloni, E. Fainelli, A. Mühleisen, and G. Stefani, *Phys. Rev. A* **49**, 1480 (1994).
- [31] P. Pelicon, I. Čadež, M. Žitnik, Ž. Šmit, S. Dolenc, A. Mühleisen, and R. I. Hall, *Phys. Rev. A* **62**, 022704 (2000).
- [32] S. H. Southworth, E. P. Kanter, B. Krässig, L. Young, G. B. Armen, J. C. Levin, D. L. Ederer, and M. H. Chen, *Phys. Rev. A* **67**, 062712 (2003).
- [33] G. Goldsztejn, T. Marchenko, R. Püttner, L. Journal, R. Guillemin, S. Carniato, P. Selles, O. Travnikova, D. Céolin, A. F. Lago *et al.*, *Phys. Rev. Lett.* **117**, 133001 (2016).
- [34] G. Goldsztejn, R. Püttner, L. Journal, R. Guillemin, O. Travnikova, B. Cunha de Miranda, I. Ismail, S. Carniato, P. Selles, D. Céolin *et al.*, *Phys. Rev. A* **96**, 012513 (2017).
- [35] W. Mehlhorn, in *Photoionization and Other Probes of Many-Electron Interactions*, edited by F. J. Wuilleumier (Plenum, New York, 1976), pp. 309–330.
- [36] H. Aksela, *J. Electron Spectrosc. Relat. Phenom.* **19**, 371 (1980).
- [37] T. W. Gorczyca and N. R. Badnell, *J. Phys. B: At., Mol., Opt. Phys.* **30**, 3897 (1997).
- [38] T. W. Gorczyca, T.-G. Lee, and M. S. Pindzola, *J. Phys. B: At., Mol., Opt. Phys.* **46**, 195201 (2013).
- [39] T. W. Gorczyca, C. P. Ballance, S. T. Manson, D. Kilcoyne, and W. C. Stolte, *Phys. Scr.* **96**, 064005 (2021).
- [40] M. H. Chen, *Phys. Rev. A* **44**, 239 (1991).
- [41] Y. Liu, J. Zeng, and J. Yuan, *J. Phys. B: At., Mol., Opt. Phys.* **46**, 145002 (2013).
- [42] Y. Li, L. Liu, C. Gao, J. Zeng, and J. Yuan, *J. Electron Spectrosc. Relat. Phenom.* **226**, 26 (2018).
- [43] S. Carniato, *J. Electron Spectrosc. Relat. Phenom.* **239**, 146931 (2020).
- [44] M. D. Kiselev, E. V. Gryzlova, S. M. Burkov, O. Zatsarinny, and A. N. Grum-Grzhimailo, *Atoms* **9**, 114 (2021).
- [45] L. Young, E. P. Kanter, B. Krässig, Y. Li, A. M. March, S. T. Pratt, R. Santra, S. H. Southworth, N. Rohringer, L. F. DiMauro *et al.*, *Nature (London)* **466**, 56 (2010).
- [46] D. Céolin, J. Ablett, D. Prieur, T. Moreno, J.-P. Rueff, T. Marchenko, L. Journal, R. Guillemin, B. Pilette, T. Marin *et al.*, *J. Electron Spectrosc. Relat. Phenom.* **190**, 188 (2013).
- [47] D. A. Walko, B. W. Adams, G. Doumy, E. M. Dufresne, Y. Li, A. M. March, A. R. Sandy, J. Wang, H. Wen, and Y. Zhu, in *Proceedings of the 12th International Conference on Synchrotron Radiation Instrumentation—SRI2015*, edited by Q. Shen and C. Nelson, AIP Conf. Proc. No. 1741 (AIP, New York, 2016), p. 030048.
- [48] A. Albiez, M. Thoma, W. Weber, and W. Mehlhorn, *Z. Phys. D: At. Mol. Clusters* **16**, 97 (1990).
- [49] V. Schmidt, *Electron Spectrometry of Atoms using Synchrotron Radiation* (Cambridge University Press, Cambridge, UK, 1997).
- [50] S. Svensson, B. Eriksson, N. Mårtensson, G. Wendin, and U. Gelius, *J. Electron Spectrosc. Relat. Phenom.* **47**, 327 (1988).
- [51] P. G. Burke, *R-matrix Theory of Atomic Collisions* (Springer, New York, 2011).
- [52] K. A. Berrington, W. B. Eissner, and P. H. Norrington, *Comput. Phys. Commun.* **92**, 290 (1995).
- [53] <http://amdpp.phys.strath.ac.uk/tamoc/>.
- [54] Connorb.freeshell.org.
- [55] M. J. Seaton, *Philos. Trans. R. Soc. London A* **245**, 469 (1953).
- [56] P. G. Burke, D. F. Gallaher, and S. Geltman, *J. Phys. B: At. Mol. Phys.* **2**, 1142 (1969).
- [57] J. H. McGuire, N. Berrah, R. J. Bartlett, J. A. R. Samson, J. A. Tanis, C. L. Cocke, and A. S. Schlachter, *J. Phys. B: At., Mol., Opt. Phys.* **28**, 913 (1995).
- [58] K. Bartschat, E. T. Hudson, M. P. Scott, P. G. Burke, and V. M. Burke, *J. Phys. B: At., Mol., Opt. Phys.* **29**, 115 (1996).
- [59] K. Bartschat, E. T. Hudson, M. P. Scott, P. G. Burke, and V. M. Burke, *Phys. Rev. A* **54**, R998(R) (1996).
- [60] P. J. Marchalant and K. Bartschat, *Phys. Rev. A* **56**, R1697 (1997).
- [61] D. C. Griffin, C. P. Ballance, and M. S. Pindzola, *Phys. Rev. A* **80**, 023420 (2009).
- [62] D. C. Griffin, M. S. Pindzola, C. P. Ballance, and J. Colgan, *Phys. Rev. A* **79**, 023413 (2009).
- [63] J. Colgan, D. C. Griffin, C. P. Ballance, and M. S. Pindzola, *Phys. Rev. A* **80**, 063414 (2009).
- [64] O. Zatsarinny, *Comput. Phys. Commun.* **174**, 273 (2006).
- [65] A. Kramida, Yu. Ralchenko, J. Reader, and NIST ASD Team, National Institute of Standards and Technology, 2022, <http://physics.nist.gov/asd>.
- [66] J. A. R. Samson, G. H. Rayborn, and P. N. Pareek, *J. Chem. Phys.* **76**, 393 (1982).
- [67] D. A. Verner and D. G. Yakovlev, *Astron. Astrophys. Suppl. Ser.* **109**, 125 (1995).
- [68] B. H. Bransden and C. J. Joachain, *Physics of Atoms and Molecules* (Prentice Hall, Pearson Education, New York, 2014).
- [69] S. T. Manson, in *The Physics of Electronic and Atomic Collisions*, edited by A. Dalgarno, R. S. Freund, P. M. Koch, M. S. Lubell, and T. B. Lucatorto, AIP Conf. Proc. No. 205 (AIP, New York, 1990), pp. 189–200.